JOURNAL OF GEOPHYSICAL RESEARCH, VOL. 102, NO. B10, PAGES 22,391–22,409, OCTOBER 10, 1997

Time dependent inversion of geodetic data

Paul Segall

Department of Geophysics, Stanford University, Stanford, California

Mark Matthews

Department of Mathematics, Massachusetts Institute of Technology, Cambridge

Abstract. The recent expansion of permanent Global Positioning System (GPS) networks provides crustal deformation data that are dense in both space and time. While considerable effort has been directed toward using these data for the determination of average crustal velocities, little attention has been given to detecting and estimating transient deformation signals. We introduce here a Network Inversion Filter for estimating the distribution of fault slip in space and time using data from such dense, frequently sampled geodetic networks. Fault slip is expanded in a spatial basis set $\mathcal{B}_k(\mathbf{x})$ in which the coefficients are time varying, $s(\mathbf{x},t) = \sum_{k=1}^{M} c_k(t)\mathcal{B}_k(\mathbf{x})$. The temporal variation in fault slip is estimated nonparameterically by taking slip accelerations to be random Gaussian increments, so that fault slip is a sum of steady state and integrated random walk components. A state space model for the full geodetic network is formulated, and Kalman filtering methods are used for estimation. Variance parameters, including measurement errors, local benchmark motions, and temporal and spatial smoothing parameters, are estimated by maximum likelihood, which is computed by recursive filtering. Numerical simulations demonstrate that the Network Inversion Filter is capable of imaging fault slip transients, including propagating slip events. The Network Inversion Filter leads naturally to automated methods for detecting anomalous departures from steady state deformation.

1. Introduction

In the past 10 years there has been a tremendous increase in the number and density of geodetic networks for the study of crustal deformation. In particular the dramatic decrease in the cost of Global Positioning System (GPS) receivers has led to a number of large permanent GPS arrays, including the Southern California Integrated GPS Network (SCIGN) [*Bock et al.*, 1993; *Blewitt et al.*, 1993], the San Francisco Bay Area Regional Deformation (BARD) network [*King et al.*, 1995], and two large networks in Japan, the GPS Regional Array for Precise Surveying (GRAPES), and the Continuous Strain Monitoring System (COSMOS) [*Shimada and Bock*, 1992; *Miyazaki et al.*, 1996]. Smaller regional GPS networks have also been in operation in the Pacific Northwest [*Dragert and Hyndman*, 1995], the Big Island of Hawaii [*Lisowski et al.*, 1996], and elsewhere. While most of the recent growth has been in GPS networks, frequently monitored dual-frequency geodimeter networks have been in operation in Parkfield [*Langbein et al.*, 1990] and the Long Valley caldera [*Langbein et al.*, 1995] for the last decade.

Permanent GPS networks yield daily estimates of site positions with a precision of a few millimeters in the horizontal components over regional distances [e.g., *Heflin et al.*, 1992; *King et al.*, 1995]. Precision is generally a factor of 3 poorer in the vertical component. Initially, permanent GPS networks incorporated relatively few widely spaced receivers, and thus sacrificed spatial coverage for improved temporal resolution [e.g., *Shimada and Bock*, 1992; *Dragert and Hyndman*, 1995]. However, the situation is now changing rapidly. The Japanese GPS network currently consists of 610 permanent GPS stations, with a station spacing of $\sim$ 30 km nationwide and a greater concentration in the Kanto-Tokai area. Plans for the southern California (SCIGN) array call for expansion from the current 40 station network to as many as 250 permanent GPS receivers. With these developments we now, or shall soon, have available deformation data that are dense in both space and time.

Continuously operating GPS arrays have recorded coseismic displacements from a number of earthquakes [e.g., *Bock et al.*, 1993; *Blewitt et al.*, 1993; *Tsuji et al.*, 1995]. These step discontinuities in the GPS time series are reasonably easy to detect and quantify, and the

Paper number 97JB01795.
0148-0227/97/97JB-01795$09.00

measured displacements can be used to invert for the spatial distribution of fault slip [e.g., *Barrientos and Ward*, 1990; *Árnadóttir and Segall*, 1994;*Freymueller et al.*, 1994; *Wald and Heaton*, 1994; *Bennett et al.*, 1995].

These networks also provide precise measurements of the average interseismic velocity field. Interseismic deformation, as measured over the past two decades with terrestrial geodimeters, is very nearly steady in time [e.g., *Savage and Lisowski*, 1995]. In part because these measurements were most often collected annually, the existence of transient interseismic deformations has been difficult to separate from possible time-varying systematic measurement errors [e.g., *Savage and Lisowski*, 1995]. Evidence for transient interseismic deformation has been reported [e.g., *Jachens et al.*, 1983], particularly in or near the creeping section of the San Andreas fault [*Langbein et al.*, 1990; *Linde et al.*, 1996]. Of course, transient postseismic deformations following earthquakes are well known [e.g., *Prescott et al.*, 1984; *Savage et al.*, 1994; *Shen et al.*, 1994; *Bürgmann et al.*, 1997]. Deformation in volcanic areas is also notably nonsteady [e.g., *Shimada et al.*, 1990; *Langbein et al.*, 1995].

Given station velocities, or in the case of geodimeter measurements the rates of baseline length change, it is possible to invert for the spatial distribution of fault slip rate [e.g., *Segall and Harris*, 1986; *Harris and Segall*, 1987; *Johnson*, 1993; *Fukahata et al.*, 1996]. Daily position determinations can provide much richer information than simply the average velocity. In fact, with data from frequently sampled, dense geodetic networks, it is now possible to address questions such as, What is the slip rate pattern on faults in space and time? Are there slip waves that propagate aseismically at depth? What is the source time history of slow earthquakes? Does the pattern of aseismic slip rate change before large earthquakes? Rather than determine images of average slip rate (as, for example, in the work of *Segall and Harris* [1986]) we wish to determine the full space time history of fault slip rate, in essence, to make movies of the slip rate pattern.

There are major difficulties in time dependent inversions for slip rate. First, we do not know a priori the nature of the temporal variations for which we are searching. Second, geodetic measurements contain spatially and temporally correlated errors, due, for example, to atmospheric path delays, multipath, and random benchmark motions [e.g., *Wyatt*, 1982, 1989]. Considerable attention has been focused on the fact that local monument motions substantially increase the uncertainty in estimates of average velocity [*Johnson and Agnew*, 1995]. Local monument motions also complicate the detection of transient crustal motions. Thus, any viable estimation procedure must allow for general, nonparametric estimation of the temporal variations in fault slip and account for correlated errors in the observations.

We present here a time domain filtering approach to this problem, based on earlier work [*Matthews and Segall*, 1988; *Matthews* , 1991], that analyzes data from the complete geodetic network, rather than baseline by baseline. Analyzing all the data simultaneously allows one to separate time-varying tectonic signals from local monument motions. Time domain filtering leads naturally to automated methods for detecting changes in the underlying slip rates. That automated methods are required is obvious when one considers that, for example, the 600-station Japanese network already produces 2×10^5 three-dimensional positions per year.

We begin by briefly summarizing the method as described in the following section. Given a collection of deformation time series, we expand the source model in a set of basis functions. We then pose a Gaussian model for the time-varying coefficients of these functions that enforces an a priori expectation that the source process is steady state. We further pose Gaussian models for local benchmark motions and observation errors at each site. Recursive linear (Kalman) filtering is used to estimate system processes at times of interest given all past and present data and to forecast future observations. The scale parameters of the various Gaussian processes are estimated by maximum likelihood. The approach outlined here has the following properties: (1) It enables separation of spatially coherent signals from local motions; (2) it allows for real time anomaly detection; (3) it handles arbitrary timing, location, and type of observation; and (4) the recursive algorithm is computationally efficient, providing optimal estimates while obviating the need to solve huge systems of linear equations.

2. Method

We model displacements at the Earth's surface $u_r(\mathbf{x},t)$ as a function of spatial coordinate $\mathbf{x}$ and time t by

$$u_r(\mathbf{x},t) = \int_\Sigma s_p(\boldsymbol{\xi},t) G^r_{pq}(\mathbf{x},\boldsymbol{\xi}) \mathbf{n}_q(\boldsymbol{\xi}) d\Sigma(\boldsymbol{\xi}) + \mathcal{L}(\mathbf{x},t) + \epsilon. \quad (1)$$

The three terms on the right side of (1) represent the underlying deformation signal, local benchmark motion, and measurement error, respectively. In (1), and throughout this paper, we assume that the true deformation can be adequately represented by some spatially and temporally varying displacement discontinuity, or slip $\mathbf{s}(\boldsymbol{\xi},t)$, across one or more planar fault surfaces in a homogeneous, isotropic, elastic half-space. Deformation at depth below the seismogenic zone may, in fact, be distributed across a fault zone of finite width, in which case the slip approximates the integrated strain across the fault. Although our focus here is on fault slip, opening mode sources (dikes) can be treated with the same procedure. We have not attempted to model distributed volume or pressure sources at this point. In (1), $p,q,r,= 1,2,3$, summation on repeated indices is implied, and $\mathbf{n}_q(\boldsymbol{\xi})$ is the unit normal to the fault surface $\Sigma(\boldsymbol{\xi})$. The $G^r_{pq}(\mathbf{x},\boldsymbol{\xi})$ are proportional to deriva-

tives of the elastostatic Green's tensors [e.g., *Aki and Richards*, 1980].

We take the measurement errors to be normally distributed with a covariance matrix that is known (for example from the GPS data processing), at least to within a scalar factor σ^2. There has been considerable discussion as to the appropriate stochastic model for local benchmark motions. *Wyatt* [1982, 1989] found that monument displacements exhibit 1/frequency^2 power spectra, indicative of a Brownian random walk process. Recent work by *Langbein and Johnson* [1997] suggest that local motions of geodetic monuments are Brownian, although other stochastic models are possible. In either case, random local motions should be spatially uncorrelated, at least at the scales (kilometers to tens of kilometers) at which geodetic stations are typically spaced, whereas tectonic motions are spatially coherent at these scales. Tectonic motions at scales less than the spacing between stations, on the other hand, may be indistinguishable from local benchmark instability.

For the purposes of this analysis we take the local motions to be Brownian with scale parameter τ

$$B(t) = \tau \int_0^t dw(t'), \tag{2}$$

where dw is formal white noise. Note that τ^2 has units length^2/time. Other nontectonic processes, such as subsidence due to large scale fluid withdrawal or extensive landsliding, are not well modeled by random benchmark motions and should be treated separately.

We take the estimated slip to be a linear combination of spatial functions $\mathcal{B}(\mathbf{x})$

$$s_p(\mathbf{x}, t) = \sum_{k=1}^{M} c_k^{(p)}(t)\mathcal{B}_k(\mathbf{x}), \tag{3}$$

where M is the number of basis functions included in the estimate. The basis functions are usually chosen in such a way that the resulting slip distribution satisfies prior expectation about the nature of the solution, for example that it is spatially smooth [*Matthews and Segall*, 1993], although the approach here is general and uniform slip bases can also be used.

Substituting the model for slip (3) into (1) yields

$$u_r(\mathbf{x}_n, t) = \sum_{k=1}^{M} c_k^{(p)}(t)F_{rk}^{(p)} + \mathcal{L}(\mathbf{x}, t) + \epsilon, \tag{4}$$

where summation on p is implied and

$$F_{rk}^{(p)} \equiv \int_\Sigma \mathcal{B}_k(\boldsymbol{\xi})G_{pq}^r(\mathbf{x}_n, \boldsymbol{\xi})\mathbf{n}_q(\boldsymbol{\xi})d\Sigma(\boldsymbol{\xi}). \tag{5}$$

If the network contains N stations with coordinates $\mathbf{x}_n$, $n = 1, 2, \ldots N$, the $3 \times N$ displacement components can be collected in a data vector $\mathbf{d}$,

$$d_i(t_j) = u_r(\mathbf{x}_n, t_j), \qquad i = 3(n-1) + r. \tag{6}$$

Letting $m = 3(k-1) + p$, we can write the observation equation in the following form

$$d_i(t_j) = \sum_{m=1}^{3M} c_m(t_j)F_{im} + \mathcal{L}_i(t_j) + \epsilon_{ij}. \tag{7}$$

Numerous geodetic measurements have shown that interseismic deformation accumulates in a nearly steady state manner [e.g., *Savage and Lisowski*, 1995]. The goal here, however, is to search for small departures from steady state deformation. Because we do not know a priori the functional form of these transients, a nonparametric description is required. Given the prior expectation that slip is nearly steady, we adopt a stochastic model in which the slip accelerations are nearly zero. If the accelerations are identically zero, then the slip velocity is constant, and relative station displacements accumulate linearly in time. Assuming the basis functions are appropriately normalized, this implies, from (3), that the $\ddot{c}_m$ are small. We thus adopt the stochastic representation

$$\ddot{c}_m(t) = w_m(t), \tag{8}$$

where $w_m(t)$ are independent white noise processes with variance α^2. Integrating (8) twice with respect to time yields

$$c_m(t) = v_m t + W_m(t) \tag{9}$$

where we assume, without loss of generality, that $c_m(t = 0) = 0$, that is, we measure accumulated slip from the time of the first observation. $W(t)$ is integrated random walk, with scale parameter α

$$W(t) = \int_0^t B(t')dt', \tag{10}$$

where α^2 has unit of length^2/time^3.

2.1 State Space Models

The stochastic equations for the local benchmark motion and the time dependence of the tectonic signal are easily modeled using state space methods. These represent a stochastic system in terms of a state vector that evolves linearly in time and is also linearly related to the data. An advantage of this method over, for example, frequency domain methods is that there is no requirement that the data be regularly sampled in time. A further advantage is that the number of observations at each measurement epoch can vary, so that missing data from a particular station (or group of stations) are easily handled.

Let $\mathbf{X}_k$ represent the state vector at epoch $t_k, k = 0, 1, 2, \ldots$. The state space model is governed by the observation equations (11) which relate the data to the state vector

$$\mathbf{d}_k = H_k\mathbf{X}_k + \epsilon_k, \qquad \epsilon_k \sim N(0, R_k), \tag{11}$$

and the state transition equation (12)

$$\mathbf{X}_{k+1} = T_{k+1}\mathbf{X}_k + \delta_{k+1}, \qquad \delta_k \sim N(0, Q_{k+1}), \tag{12}$$

which describes the evolution of the state vector due to the system dynamics.

Random walk and integrated random walk are easily represented in the state space formalism. For a random walk $\mathbf{X}_k = B(t_k)$ (equation (2)), and the state transition equation is

$$T_k = I, \qquad Q_k = \tau^2(t_k - t_{k-1}), \tag{13}$$

i.e., the state at time t_{k+1} is equal to the state at time t plus a random increment with variance proportional to the elapsed time.

The signal (9) can be modeled with the state vector

$$\mathbf{X}_k = [v, W(t_k), \dot{W}(t_k)]^T, \tag{14}$$

and

$$c(t_k) = [t_k, 1, 0]\mathbf{X}_k. \tag{15}$$

The state space model is completed by specifying the state transition matrix T_k and covariance Q_k

$$T_k = \begin{pmatrix} 1 & 0 & 0 \\ 0 & 1 & (t_k - t_{k-1}) \\ 0 & 0 & 1 \end{pmatrix} \tag{16}$$

$$Q_k = \begin{pmatrix} 0 & 0 & 0 \\ 0 & \alpha^2\frac{(t_k - t_{k-1})^3}{3} & \alpha^2\frac{(t_k - t_{k-1})^2}{2} \\ 0 & \alpha^2\frac{(t_k - t_{k-1})^2}{2} & \alpha^2(t_k - t_{k-1}) \end{pmatrix} \tag{17}$$

A simple example may be illustrative. The signal in this case is quadratic in time, while the added error process is white (Figure 1). When α is identically zero the model (9) is linear in time, and in fact the filtering procedure described below yields the least squares linear fit to the data. As α increases, the estimate becomes more oscillatory, and indeed with α very large the estimated signal fits each data point. An intermediate choice of α, however, yields a very good fit to the underlying quadratic signal. Note that it was not necessary to know that the signal is, in fact, quadratic, or even to prescribe a parametric form for the signal. It is required, however, that the temporal smoothing parameter α be chosen properly. Maximum likelihood methods for selecting α are discussed below.

The state vector for the full geodetic network is

$$\mathbf{X}_k = [v_1, W_1(t_k), \dot{W}_1(t_k), v_2, W_2(t_k), \dot{W}_2(t_k), \ldots v_M, W_M(t_k), \dot{W}_M(t_k), B_1(t_k), B_2(t_k), \ldots B_N(t_k)]^T \tag{18}$$

where M is the number of basis functions and N is the number of stations in the network. The length of the state vector is $3M+N$: three terms for each basis vector and one term for the random walk component at each station.

The state transition matrix for the Network Inversion Filter has the form

$$T_k = \begin{pmatrix} T_k^W & 0 & 0 & 0 \\ 0 & \ddots & 0 & 0 \\ 0 & 0 & T_k^W & 0 \\ 0 & 0 & 0 & I_{N\times N} \end{pmatrix} \tag{19}$$

where there are M submatrices T_k^W of the form defined by (16). The process covariance matrix is of the form

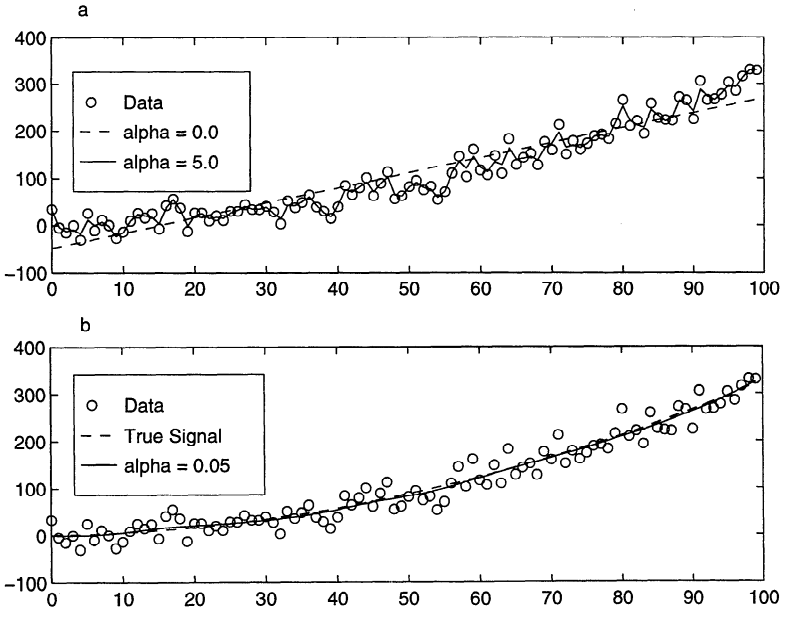

Figure 1. Simple example to illustrate nonparametric estimation of an underlying signal. Data generated by a second order polynomial with white noise added. (a) When $\alpha = 0$ the filtered estimate is exactly equivalent to a least squares fit of a straight line to the data. (Note that the linear fit systematically underpredicts the data at short and long time, and overpredicts the data at intermediate time.) With $\alpha = 5$ the estimate clearly overfits the data. (b) With an appropriate choice of α the underlying signal is reasonably approximated.

$$Q_k = \begin{pmatrix} Q_k^W & 0 & 0 & 0 \\ 0 & \ddots & 0 & 0 \\ 0 & 0 & Q_k^W & 0 \\ 0 & 0 & 0 & \tau^2(t_k - t_{k-1}) I_{N\times N} \end{pmatrix} \quad (20)$$

where there are M submatrices Q_k^W of the form defined by (17). Here we have assumed that the random walk variance is the same at all sites, which is unlikely to be true in nature. Allowing for different random walk statistics at each station is accomplished by straightforward modification of (20). This would, however, complicate maximum likelihood estimation of the variance parameters.

The observation matrix is

$$H_k = \begin{pmatrix} F & \begin{bmatrix} t_k & 1 & 0 & 0 & 0 & 0 & 0 \\ 0 & 0 & 0 & t_k & 1 & 0 & 0 \\ & & & & & & \ddots \end{bmatrix}, & I_{N\times N} \end{pmatrix} \quad (21)$$

The submatrix F, defined in (5) as the $N \times M$ matrix that maps the contribution from each basis function to the data, premultiplies the $M \times 3M$ matrix in square brackets. The $N \times N$ identity matrix maps the local benchmark motion into each observation.

Finally, the observation covariance is taken to be known to within a scalar

$$R_k = \sigma^2 \Sigma_k, \quad (22)$$

where Σ_k is an $N \times N$ matrix. In the GPS case, Σ_k is known from the GPS analysis software and includes correlations between components and stations. The need for a scale factor Σ arises because the analysis software does not fully model all error sources (multipath for example).

2.2 Filtering and smoothing

The state vector $\mathbf{X}_k$ is estimated at each state t_k by recursive linear Kalman (forward) filtering and (backward) smoothing. Let

$$\hat{\mathbf{X}}_{k\,|\,j} = E[X_k \mid \mathbf{d}_1, \ldots, \mathbf{d}_j], \quad (23)$$

$$\Sigma_{k\,|\,j} = \mathrm{Cov}[X_k \mid \mathbf{d}_1, \ldots, \mathbf{d}_j], \quad (24)$$

be the conditional mean and covariance matrix of the state at epoch k given data through epoch j. The left side of (23) is read "$\hat{\mathbf{X}}$ at epoch k given data to epoch j" or more simply "$\hat{\mathbf{X}}$ at k given j."

The conditional means and covariances satisfy the one-step-ahead prediction equations,

$$\hat{\mathbf{X}}_{k+1\,|\,k} = T_{k+1}\, \hat{\mathbf{X}}_{k\,|\,k} \quad (25)$$

$$\Sigma_{k+1\,|\,k} = T_{k+1}\, \Sigma_{k\,|\,k}\, T_{k+1}^T + Q_{k+1}, \quad (26)$$

and the update equations

$$\hat{\mathbf{X}}_{k\,|\,k} = \hat{\mathbf{X}}_{k\,|\,k-1} + G_k\, \nu_k \quad (27)$$

$$\Sigma_{k\,|\,k} = \Sigma_{k\,|\,k-1} - G_k\, H_k\, \Sigma_{k\,|\,k-1}. \quad (28)$$

Here, the innovation, or prediction residual, ν_k is the difference between the observed data at time t_k and that predicted by the state vector conditioned on data up to time t_{k-1}

$$\nu_k \equiv \mathbf{d}_k - H_k\, \hat{\mathbf{X}}_{k\,|\,k-1}, \quad (29)$$

and the Kalman gain G_k is given by

$$G_k \equiv \Sigma_{k\,|\,k-1}\, H_k^T\, (R_k + H_k\, \Sigma_{k\,|\,k-1}\, H_k^T)^{-1}. \quad (30)$$

The Kalman filter proceeds by starting with a prior estimate $\hat{\mathbf{X}}_{1\,|\,0}$ and covariance $\Sigma_{1\,|\,0}$. The prior may be "diffuse", with large uncertainty on the steady state slip v, or may reflect a priori information from previous studies. Updating the state with the first observation $\mathbf{d}_1$ using (27) and (28) leads to the posterior mean $\hat{\mathbf{X}}_{1\,|\,1}$ and associated covariance. Note that if the observation agrees exactly with that predicted by the prior the innovation is zero and the state vector does not change, although the covariance may change. The prediction equations (25) and (26) are then used to estimate $\hat{\mathbf{X}}_{2\,|\,1}$ and its covariance, and so on. The recursive filtering approach is both computationally efficient and also lends itself well to the problem of anomaly detection, as discussed below.

Having stepped through all of the data going forward in time, we end up with the conditional mean and covariance at the last epoch

$$\hat{\mathbf{X}}_{N_e\,|\,N_e} = E[\mathbf{X}_{Ne} \mid \mathbf{d}],$$

$$\Sigma_{N_e\,|\,N_e} = \mathrm{Cov}[\mathbf{X}_{Ne} \mid \mathbf{d}],$$

where N_e is the number of observation epochs. To complete the estimation procedure, we compute the posterior means and covariance of the state at all times of interest conditioned on all of the available data. This may be accomplished using the same recursive prediction and updating structure as in the filtering equations, but now going backward in time. The recursive smoothing algorithm, due to *Rauch et al.* [1965], has the form

$$\hat{\mathbf{X}}_{k\,|\,N_e} = \hat{\mathbf{X}}_{k\,|\,k} + S_k\, (\hat{\mathbf{X}}_{k+1\,|\,N_e} - \hat{\mathbf{X}}_{k+1\,|\,k}), \quad (31)$$

$$\Sigma_{k\,|\,N_e} = \Sigma_{k\,|\,k} + S_k\, (\Sigma_{k+1\,|\,N_e} - \Sigma_{k+1\,|\,k})\, S_k^T, \quad (32)$$

where the smoothing matrix at the k^{th} epoch is given by

$$S_k = \Sigma_{k\,|\,k}\, T_k^T\, \Sigma_{k+1\,|\,k}^{-1}. \quad (33)$$

2.3 Maximum Likelihood Estimation of Filter Hyperparameters

As seen from Figure 1, it is critical that the acceleration variance, or temporal smoothing parameter α^2, be chosen appropriately. It is also necessary to know or estimate the random walk scale parameter, τ^2, and the measurement variance, σ^2, from the data. Note

that with a single baseline it is difficult to distinguish between local benchmark motion and temporally varying fault slip. In other words, estimates of τ^2 and α^2 are highly negatively correlated and poorly determined. This is not true with the Network Inversion Filter, which analyzes all baselines simultaneously. Because time-varying fault slip is coherent across the network, whereas benchmark wobble is incoherent, a network analysis can distinguish between these effects.

We estimate the filter hyperparameters σ^2, τ^2, and α^2 by maximum likelihood. The likelihood is computed using a recursive filtering approach that is numerically efficient. Recursive computation of the likelihood is based on the so-called prediction-error decomposition [e.g., *Harvey,* 1981], in which the joint probability density function of N_e ordered observations is written as the product of the conditional probability density functions of each observation given the parameter $\boldsymbol{\Theta}$ and all previous observations:

$$p(\mathbf{d}_1, \ldots, \mathbf{d}_{Ne} \mid \boldsymbol{\Theta}) = \prod_{k=1}^{N_e} p_k(\mathbf{d}_k \mid \boldsymbol{\Theta}; \mathbf{d}_1, \ldots, \mathbf{d}_{k-1}). \tag{34}$$

The parameter vector $\boldsymbol{\Theta}$ has components α^2, σ^2 and τ^2. In general, the covariance matrix of the observational errors R_k is known only up to the scalar multiplier, σ^2. If the errors in the state-transition equation Q_k and the a priori variance $\Sigma_{1 \mid 0}$ can be scaled by σ^2, then we need only optimize the likelihood over α^2/σ^2 and τ^2/σ^2.

From the decomposition (34), the loglikelihood for $\boldsymbol{\Theta}$ given $\mathbf{d}$ is

$$\mathcal{L}(\boldsymbol{\Theta} \mid \mathbf{d}_1, \ldots, \mathbf{d}_{Ne}) = \sum_{k=1}^{N_e} \log[p_k(\mathbf{d}_k \mid \boldsymbol{\Theta}; \mathbf{d}_1, \ldots, \mathbf{d}_{k-1})] \tag{35}$$

For Gaussian data, the conditional probability density functions are Gaussian with mean

$$E(\mathbf{d}_k \mid \mathbf{d}_1, \ldots, \mathbf{d}_{k-1}) = \hat{\mathbf{d}}_{k \mid k-1}, \tag{36}$$

and covariances

$$E[(\mathbf{d}_k - \hat{\mathbf{d}}_{k \mid k-1})^2] = \sigma^2 V_k. \tag{37}$$

Thus the loglikelihood is

$$\mathcal{L}(\boldsymbol{\Theta}/\sigma^2 \mid \mathbf{d}) = -\frac{1}{2} N_d \log \sigma^2 - \frac{1}{2}\sum_{k=1}^{N_e} \log |V_k| - \frac{1}{2}\sigma^{-2} \sum_{k=1}^{N_e} \nu_k^T V_k^{-1} \nu_k \tag{38}$$

where N_d is the total number of data $N_d = \sum_{k=1}^{N_e} n_k$, with n_k the number of observations at each epoch. (Notice that in the filtering procedure there is no requirement that all stations be observed at every epoch.) As in (29), the ν_k are the innovations,

$$\nu_k = \mathbf{d}_k - \hat{\mathbf{d}}_{k \mid k-1} = \mathbf{d}_k - H_k \hat{\mathbf{X}}_{k \mid k-1}, \tag{39}$$

where both H_k and $\hat{\mathbf{X}}_{k \mid k-1}$ may depend on $\boldsymbol{\Theta}$. The variance of the k^{th} innovation is

$$V_k = R_k + H_k \Sigma_{k \mid k-1} H_k^T. \tag{40}$$

From (38) the maximum likelihood estimate of σ^2 is

$$\hat{\sigma}^2 = \frac{1}{N_d} \sum_{k=1}^{N_e} \nu_k^T V_k^{-1} \nu_k. \tag{41}$$

Substituting (41) into (38) yields

$$\mathcal{L}(\boldsymbol{\Theta}/\sigma^2 \mid \mathbf{d}) = -\frac{1}{2}(N_d - N_d \log N_d) - \frac{1}{2}\sum_{k=1}^{N_e} \log |V_k| - \frac{1}{2} N_d \log \left[\sum_{k=1}^{N_e} \nu_k^T V_k^{-1} \nu_k \right] \tag{42}$$

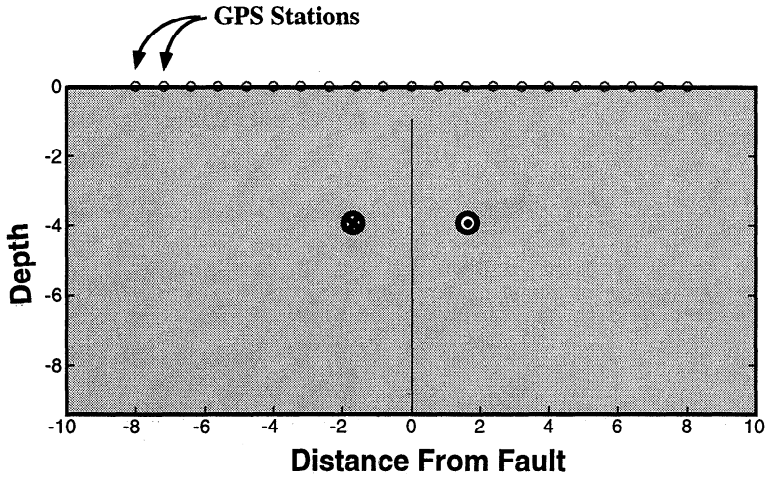

Figure 2. Geometry of locked strike-slip fault. Fault is locked from surface to depth D. Depth and distance are scaled by D. Below D the fault slips at a rate $\dot{s}(t)$. An array of displacement sensors form an array across the fault.

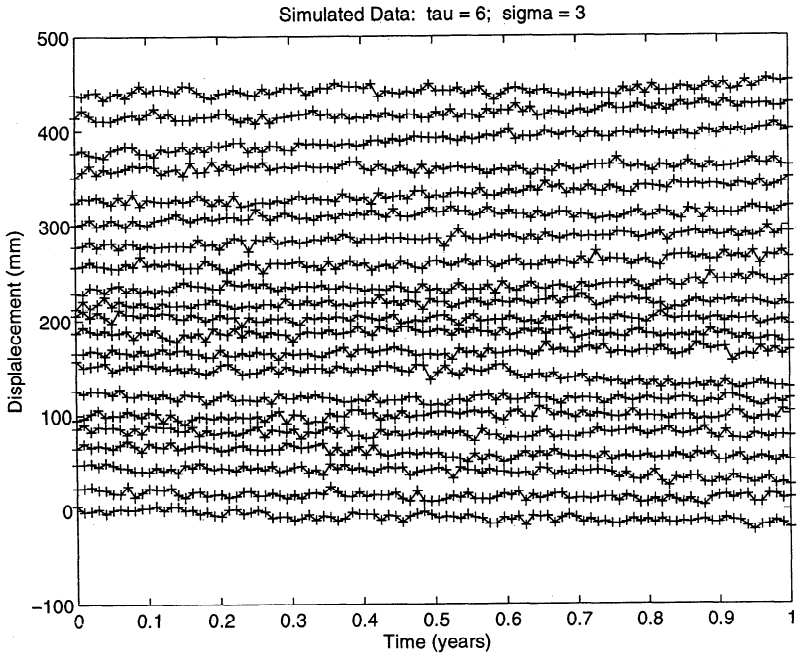

Figure 3. Simulated data over a buried strike-slip fault, with $\sigma = 3$ mm and $\tau = 6$ mm/yr$^{\frac{1}{2}}$. There are 41 baselines total; only the 21 baselines closest to the fault are shown, from west to east, with origins offset vertically for clarity.

3. Estimating Temporally Varying Slip Rate

We consider first a simple example of an infinitely long strike-slip fault locked from the surface to depth D (Figure 2). Below that depth the fault slips everywhere at rate $\dot{s}(t)$. The problem is one of antiplane strain, that is, the only non-zero displacement is u_3, which varies as a function of x_1 and x_2 only. The displacement rate at the Earth's surface is well known to be

$$\dot{u}_3(x_2 = 0, t) = \frac{\dot{s}(t)}{\pi} \tan^{-1}(\frac{x_1}{D}). \qquad (43)$$

Consider a linear array of stations which stretch across the fault in the range $-8D \leq x_1 \leq 8D$. In the simulation presented here, there are 41 stations in the array. Simulated data (Figure 3) are generated from the underlying slip history $s(t)$ with added measurement error, $\sigma = 3$ mm, and random walk local benchmark motion with $\tau = 6$ mm/yr$^{\frac{1}{2}}$. Note that while it is possible to discern the linear trends in the data, possible changes in the rate of deformation are difficult to detect by eye.

The first step in the analysis is to estimate the filter hyperparameters, σ^2, τ^2, and α^2, by maximum likelihood. Numerical calculations of the likelihood for a range of τ/σ and α/σ verify that these parameters are essentially uncorrelated, indicating that the Network Inversion Filter can distinguish between random benchmark motion and time-varying slip. This result simplifies the task of computing maximum likelihood estimates considerably, since one need only conduct two univariate optimizations in the two coordinate directions to find the optimal values.

Figure 4a shows minus twice the log likelihood ($-2\mathcal{L}$), as a function of τ, for $\alpha = 0$. The corresponding estimates of σ are shown in Figure 4b, which shows that the estimates of σ decrease with increasing τ. Ten values were computed, with the minimum corresponding to the maximum likelihood estimate. As seen from Figure 4, even this crude approach to optimization yields estimates that are in excellent agreement with the true values.

With this estimate of τ/σ held fixed, we next compute $-2\mathcal{L}$ as a function of α (Figure 5). A clear minimum in $-2\mathcal{L}$ exists corresponding to $\hat{\alpha} = 23.5$. We also compare the maximum likelihood estimate of α with the "optimal" estimate, where optimal is defined as minimizing the root-mean-square difference between the true and estimated slip rate (Figure 5b). In this example the optimal value of α is slightly greater than the maximum likelihood estimate, corresponding to a somewhat more oscillatory slip rate. When analyzing actual, rather than simulated, data we will necessarily rely on the maximum likelihood estimates of α. The previous simulations suggest that these estimates may be close to optimal.

Given estimates $\hat{\alpha}$, $\hat{\tau}$, and $\hat{\sigma}$, it is possible to compute smoothed estimates of the slip history. Figure 6 compares the estimated slip and slip rate histories with the true process. Despite the fact that the signal is not at all obvious in the raw time series (Figure 3), and that the filter has no prior knowledge of the character of the signal, the Network Inversion Filter does a good job of recovering the true, exponentially increasing, slip history.

The smoothed slip rate significantly underestimates

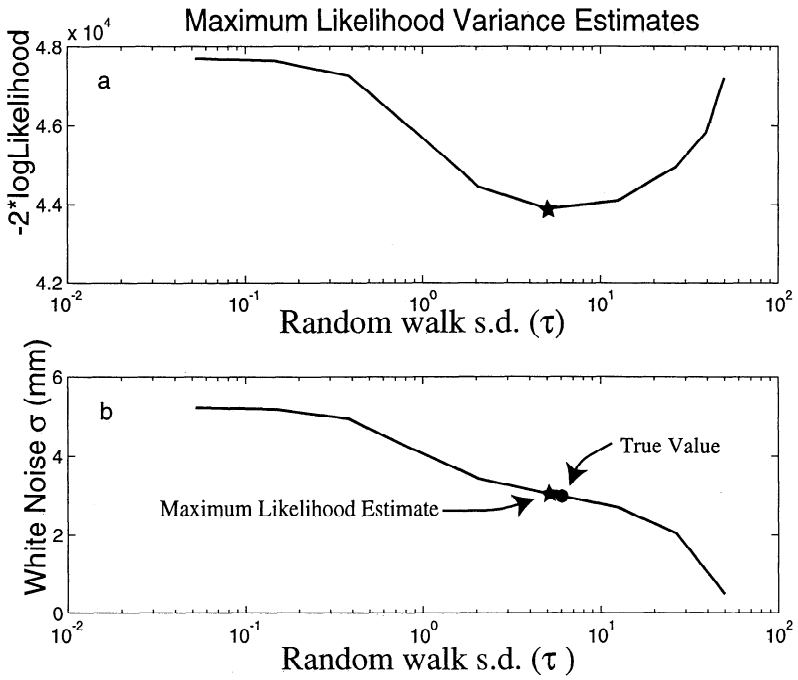

Figure 4. (a) Plot of $-2\mathcal{L}$ as a function of random walk parameter τ for the data set shown in Figure 3. The maximum likelihood estimate (minimum of $-2\mathcal{L}$) is shown with the star. (b) Corresponding estimate of σ. The maximum likelihood estimate is shown with the star and the correct values with the closed circle.

the rapid rise in slip rate at the end of the year, even considering the formal uncertainties in the smoothed estimate. This occurs because the smoothed covariance (equation (32)) does not include uncertainties in the filter hyperparameters, notably α. To get a better idea of how $\hat{\alpha}$ affects the estimated slip rate history, we compute results for three values of α, including the maximum likelihood estimate (Figure 7). Increasing α to 39, which according to Figure 5b is nearly optimal, results in a more oscillatory slip rate that somewhat better fits

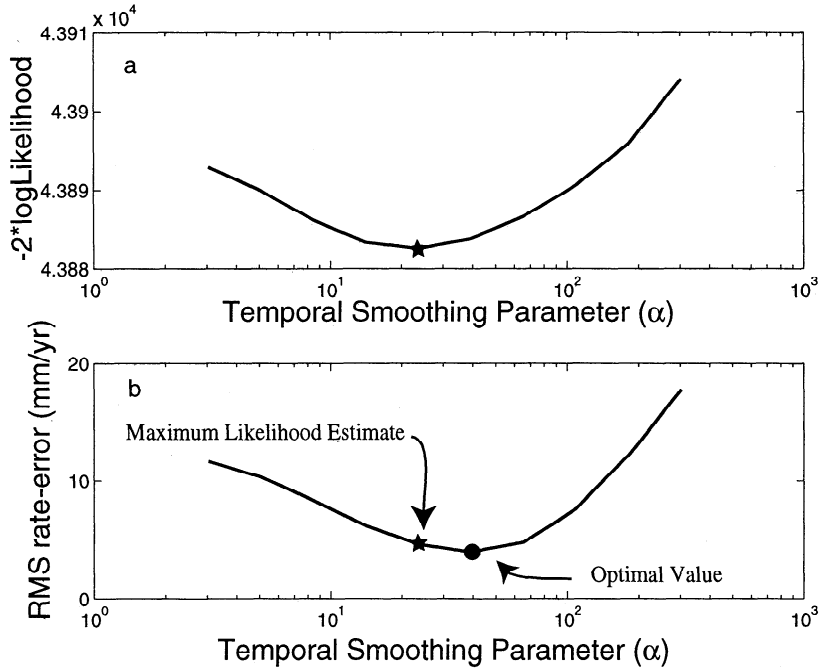

Figure 5. (a) Plot of $-2\mathcal{L}$ as a function of the temporal smoothing parameter α for the data set shown in Figure 3. The maximum likelihood estimate (star at minimum of $-2\mathcal{L}$) occurs at $\hat{\alpha} = 23.5$. (b) Root-mean-square error in the slip rate as a function of α. While the maximum likelihood estimate is nearly optimal, a slightly larger value of α would decrease the root-mean-square rate error slightly.

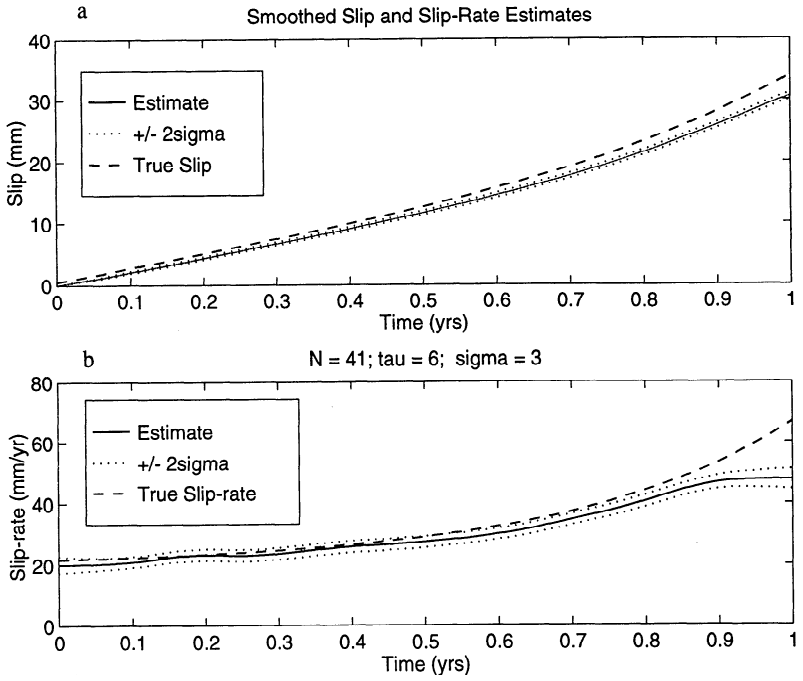

Figure 6. Comparison of the the estimated (a) slip and (b) slip rate histories with the true underlying process. Smoothed estimates are shown with 2 standard deviation confidence intervals.

the true slip rate toward the end of the year. Decreasing α to 14 flattens the slip rate and results in a poorer fit to the true slip rate.

The power of full network filtering in recovering the underlying signal is illustrated by considering simulated data from two neighboring stations (Figure 8). This figure shows the decomposition of the observed data into signal, local benchmark motion, and measurement error as in (1). Recall that the Network Inversion Filter equations specify that the local benchmark motions are spatially incoherent, whereas the signal arises from fault slip in an elastic medium, and is thus spatially coherent across the network. Thus, the smoothed estimate is able to distinguish the underlying coherent signal, even though the two data series are significantly different. Note that in some cases the estimated signal does not even "go through the data", because it must also be consistent with data from the entire network, not just a single station.

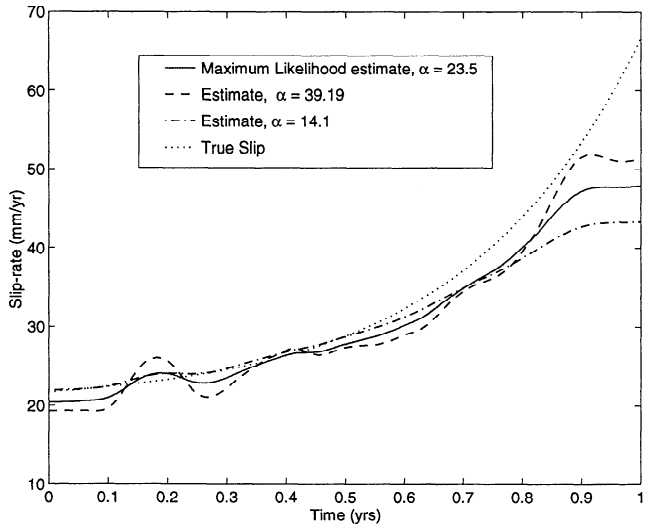

Figure 7. Estimates of slip rate as a function of time for different values of the temporal smoothing parameter α. The solid curve shows the estimate corresponding to the maximum likelihood estimate of α. For a slightly larger value of α the estimated slip rate oscillates too much about the true slip rate. For a slightly smaller value of α the estimated slip rate does not fully recover the increase in slip rate near the end of the year.

4. Slip Rate Anomaly Detection

Time domain filtering methods are not only able to estimate past fault slip histories, but they also lead rather naturally to alarm, or anomaly, detectors. As the previous example illustrates, it can be difficult to visualize transient signals by eye in data from a large array, especially if one wants to associate the transients with an inferred fault slip process. When one considers the Japanese national GPS network already produces 2×10^5 positions per year, it is easy to see that automated procedures are needed to assess whether changes in the style of crustal deformation have taken place. Time domain filtering is ideal for this because the formulae consist of repeated predictions and updates. That is, one is continually predicting the next state, conditioned on all past data, and then comparing with the next set of observations. When the new data differ significantly from the prediction, this is a natural indicator of a change in the underlying process.

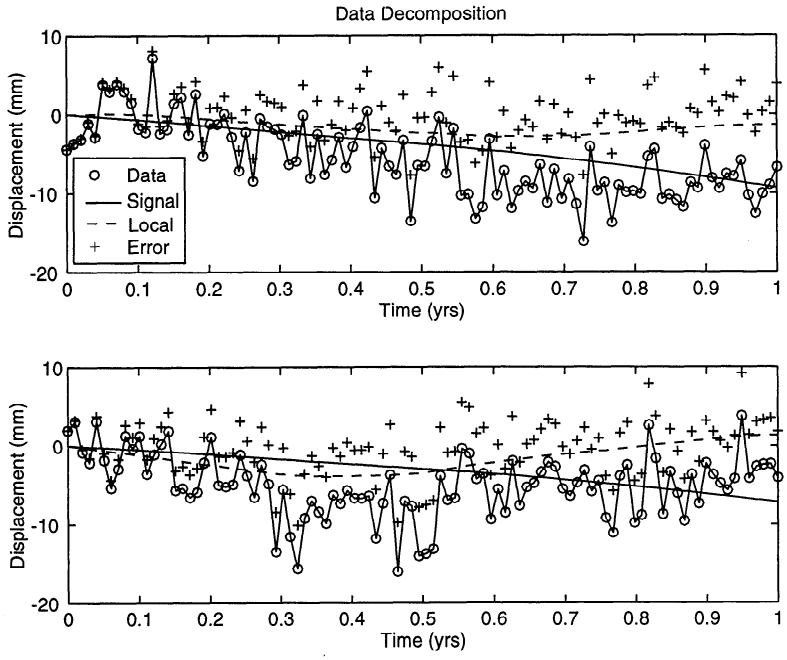

Figure 8. Decomposition of two neighboring baselines into signal, local benchmark motion, and measurement error. Notice that the estimated signal at the two sites is very similar even though the time data series are significantly different. The differences are due to the different local benchmark motions and measurement errors at the two stations. The signal is coherent between stations.

As an example we generated three years of synthetic data with constant slip rate (at 20 mm/yr) for the first two years, but with an exponentially increasing signal added in the third (Figure 9). In this example the measurement error (σ) is 3 mm, and the scale of the random benchmark motions (τ) is 4 mm /yr$^{\frac{1}{2}}$. We imagine that the first two years of data would be used to estimate the variance parameters σ^2, τ^2, and α^2. Based on these estimates one could predict the expected slip rate for the following year. We then compare the filtered estimates

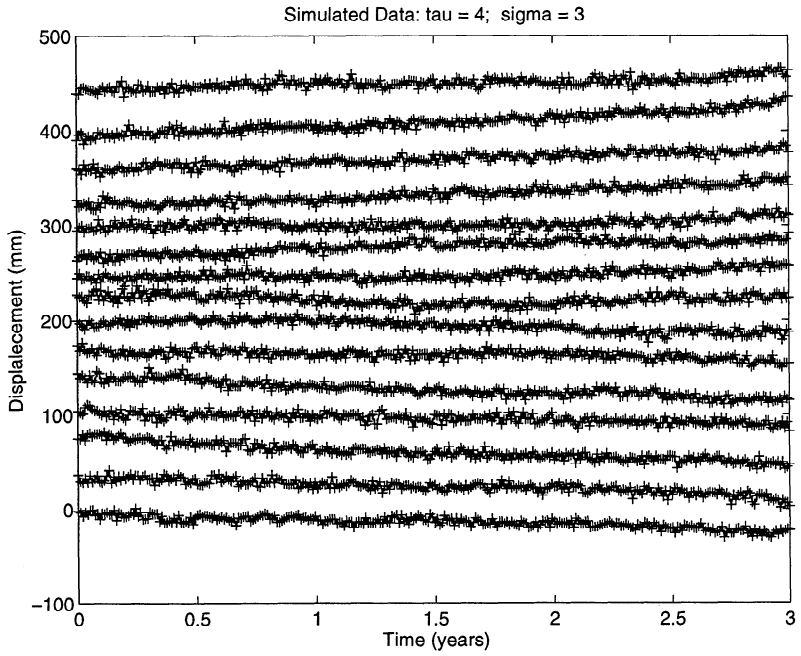

Figure 9. Simulated data over a buried strike-slip fault. For the first two years the slip rate is constant; an increasing exponential is added in the third year. Here $\sigma = 3$ mm and $\tau = 4$ mm/yr$^{\frac{1}{2}}$. There are 41 baselines total; only the 15 baselines closest to the fault are shown, from west to east, with origins offset vertically for clarity.

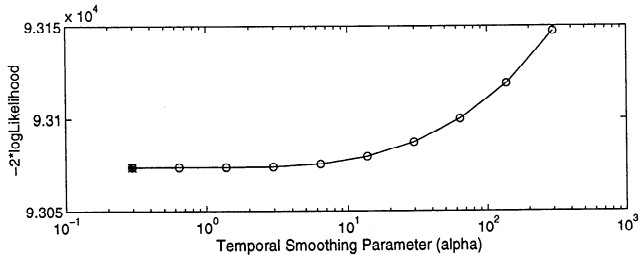

Figure 10. Minus twice the logarithm of the likelihood ($-2\mathcal{L}$) as a function of temporal smoothing parameter α for the first two years of data shown in Figure 9. Note that $-2\mathcal{L}$ monotonically increases with α when the underlying slip rate is constant.

with the prediction to determine how long it takes for the Network Inversion Filter to determine that the fault slip rate has increased.

The procedure follows that described previously, except that when the underlying slip rate is constant -2 times the logarithm of the likelihood ($-2\mathcal{L}$) is flat for small α and rises for larger α (Figure 10). This indicates that the data are consistent with a constant rate process ($\alpha = 0$), but are adequately modeled so long as α is sufficiently small. In this case the predicted slip rate for the first two years is essentially steady for α less than ~ 5. To avoid missing potential variations in slip rate, we choose $\hat{\alpha} = 3$.

The first two years of data were filtered and smoothed using the estimated $\hat{\tau}$ and $\hat{\alpha}$. The prediction equations (12) were then used to forecast the slip rate in the third year. Because the prior expectation of the Network Inversion Filter is that fault slip is a constant rate process, the predicted slip rate is constant, with uncertainty that increases with time depending on α (Figure 11). The greater the acceleration variance α, the more rapidly the slip rate uncertainty increases with time.

The filter was then initiated on data from the third year, using the state at end of year two ($t = 2$) as a prior. We again use $\hat{\alpha} = 3$. Figure 11 compares the smoothed estimates (for $0 < t < 2$ years) and the predictions (for $2 < t < 3$ years) with the filtered estimates (using (27) and (28)) for the third year. In the anomaly detection mode the Network Inversion Filter outputs estimates conditional only on data up to the present epoch, whereas in the previous example the slip rate was smoothed (i.e., conditioned on all of the data).

The filtered slip rate estimate increases steadily, and significantly exceeds the forecast slip rate at the 3 standard deviation level for roughly $t > 2.9$ years. This indicates that there is a significant increase in estimated fault slip rate relative to the previous two years. Thus, for this example, the filter is able to detect a significant change in slip rate after roughly 0.9 years.

The choice of temporal smoothing parameter α deserves some discussion. If α is chosen to be too large, the uncertainties in the predictions grow very rapidly

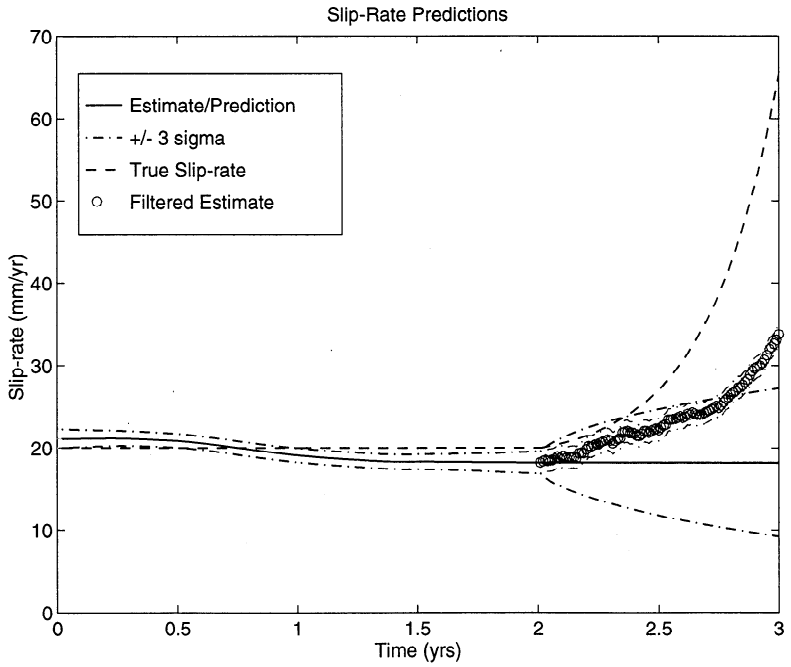

Figure 11. Ability of the Network Inversion Filter to detect an anomalous increase in fault slip rate. Smoothed slip rate estimates are shown for the first two years of data from Figure 9 ("estimate") along with 3 standard deviation error bounds. The slip rate is then predicted for the third year ("prediction") based on the state at the end of the second year. At the beginning of the third year, filtered estimates (conditional on data only up to that point) are shown ("filtered estimate"), along with 3 standard deviation error bounds. Notice that at $t \sim 2.9$ years, the filtered and predicted slip rates are different at the 3σ level, indicating that a significant increase in slip rate had occurred.

and a huge change in underlying slip rate would be required to fall outside the confidence bounds of the predictions. On the other hand, if the choice of α is too small during the filtering stage, the estimates are forced to be nearly steady and the model may not fit the data. In an actual situation in which a change in slip rate was suspected, the acceleration variance could be reestimated using additional data to determine whether α should be increased. Doing so would improve the filter performance when tracking the growing slip rate transient.

5. Inversion for Variable Fault Slip in Space and Time

We consider now true space-time inversions, in which the fault slip depends both on time and spatial coordinate on the fault surface $s(\mathbf{x}, t)$. The inverse problem, which is well known to be nonunique, is regularized by seeking solutions that minimize some norm of the slip. A number of regularizing norms can be used (see, for example, *Matthews and Segall* [1993] for a discussion in the context of antiplane slip on a vertical fault). Assuming that an appropriate norm and inner product are defined

$$||s(\mathbf{x})||^2 \equiv < s, s >, \tag{44}$$

where angle brackets denote inner product, such that the set of admissible solutions to the inverse problem defines a Hilbert space, and that the observation equations (1) are bounded linear functionals, then the forward problem can always be written in the form of an inner product

$$d_i(t_j) =< s(\xi, t_j), \Phi_i(\xi) > + \mathcal{L}_i(t_j) + \epsilon_{ij} \quad i = 1, 2, \ldots N, \tag{45}$$

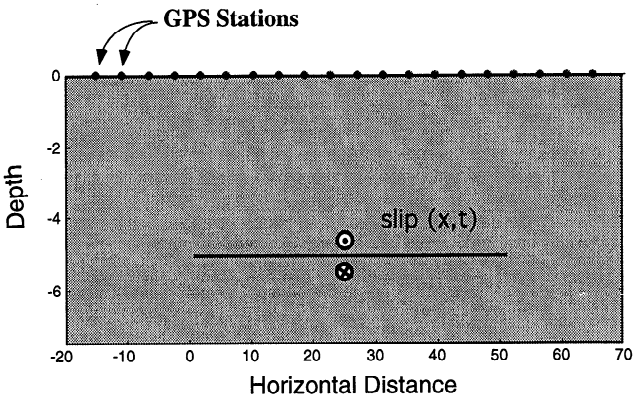

Figure 12. Geometry of horizontal detachment fault. Fault depth is D and extends for $0 < x_1 < L$. Fault slip is antiplane and varies with lateral distance and time $s(x_1, t)$. An array of GPS instruments extends from $-3D < x_1 < L + 3D$.

where the $\Phi_i(\xi)$ are known as "representers", and N is the number of observing stations in the network.

The regularized inverse problem is thus to minimize the norm of the fault slip $||s(\mathbf{x})||$, subject to the constraint that the residual norm be less than some threshold. The solution is in the form of a linear combination of the representers Φ_i [*Matthews and Segall*, 1993; *Parker*, 1994]. Here, rather than use the representers as basis functions, we define related orthobasis functions, as follows. The Gram matrix is defined as the inner product of the representers, with components

$$\Gamma_{ij} =< \Phi_i, \Phi_j > . \tag{46}$$

Expressing the Gram matrix as $\Gamma = U \Lambda U^T$, where Λ is a diagonal matrix of eigenvalues ($\Lambda =$

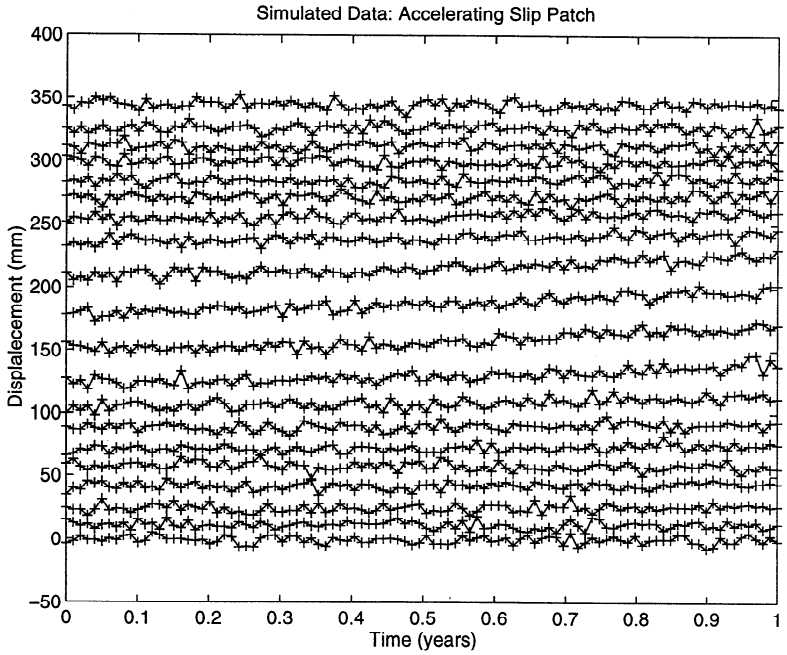

Figure 13. Simulated data over horizontal decollement. Here $\sigma = 3$ mm and $\tau = 1$ mm/yr$^{\frac{1}{2}}$. There are 20 baselines total, shown, from west to east, with origins offset vertically for clarity.

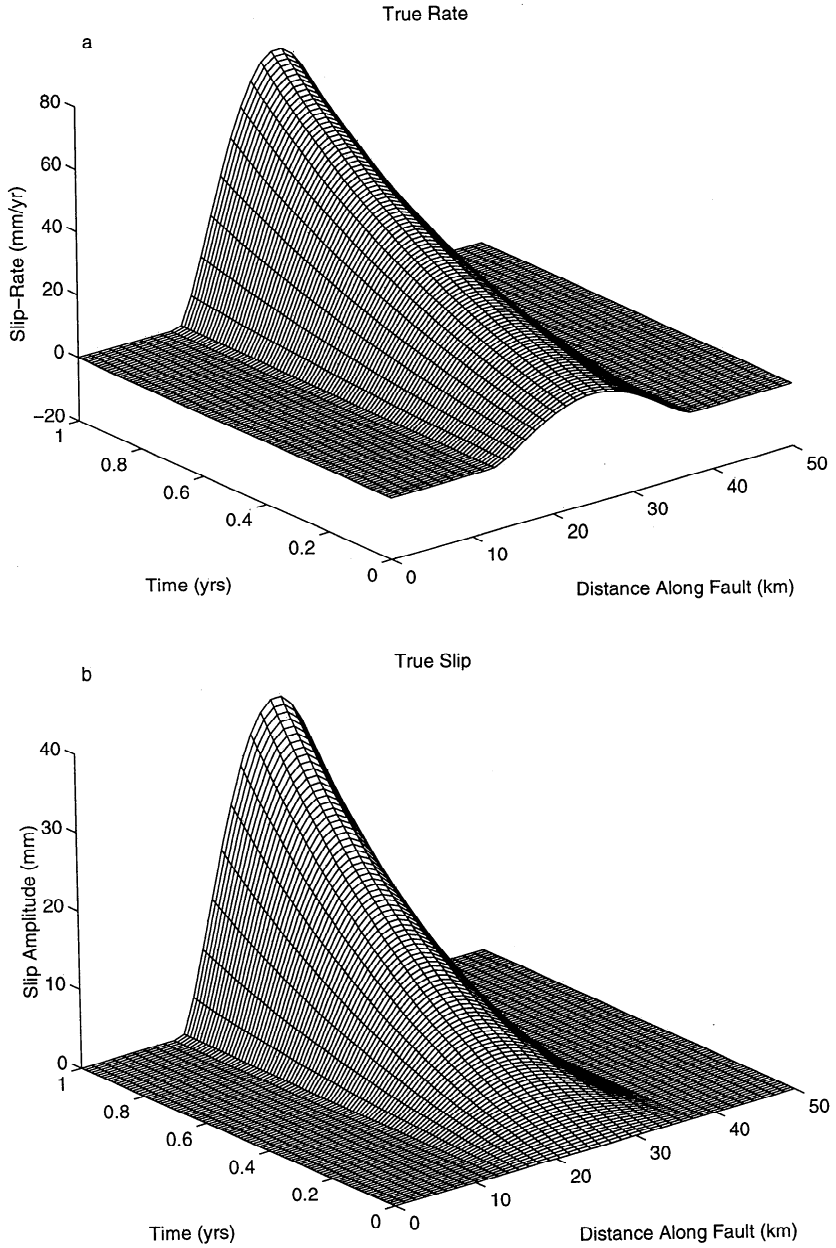

Figure 14. Growing slip event on a horizontal decollement. (a) True slip rate. (b) True slip.

$diag(\lambda_1, \lambda_2, \ldots \lambda_N)$ with $\lambda_1 > \lambda_2 > \ldots \lambda_N)$, and U an orthogonal matrix of eigenvectors. This decomposition allows one to define orthobasis functions as

$$\mathcal{B}_i = \sum_{j=1}^{N} U_{ji} \Phi_j \tag{47}$$

The slip is reconstructed from a linear combination of the orthobasis functions, as in (3), where the coefficients $c_k(t)$ are estimated via the filtering equations. The observation equation (7) thus takes the form, making use of (3), (45), and (47),

$$\mathbf{d}(t) = U\Lambda\mathbf{c}(t) + \mathcal{L}(t) + \epsilon. \tag{48}$$

Thus, the matrix that maps the contributions from each basis function to the observations in (21) is given by $F = U\Lambda$.

Given the bases $\mathcal{B}_i$, the spatial squared norm of the solution, from (3), (46), and (47), is

$$< s, s >= \mathbf{c}^T \Lambda \mathbf{c}. \tag{49}$$

This demonstrates that the orthobasis functions corresponding to the largest eigenvalues make the largest contribution to the solution norm. In the context of the Bayesian Network Inversion Filter, spatial smoothing enters through the prior state vector, $\hat{\mathbf{X}}_{1\,|\,0}$, and associated covariance, $\Sigma_{1\,|\,0}$. Given the a priori expectation that the solution norm is small, we set the prior state vector, $\hat{\mathbf{X}}_{1\,|\,0} = \mathbf{0}$, where $\mathbf{0}$ is a zero vector of length $3M + N$. Based on (49) the corresponding covariance is

$$\Sigma_{1\,|\,0} = \gamma^2 diag(1/\lambda_1, 0, 0, 1/\lambda_2, 0, 0 \ldots 1/\lambda_N, 0, 0, \mathbf{0}_N), \tag{50}$$

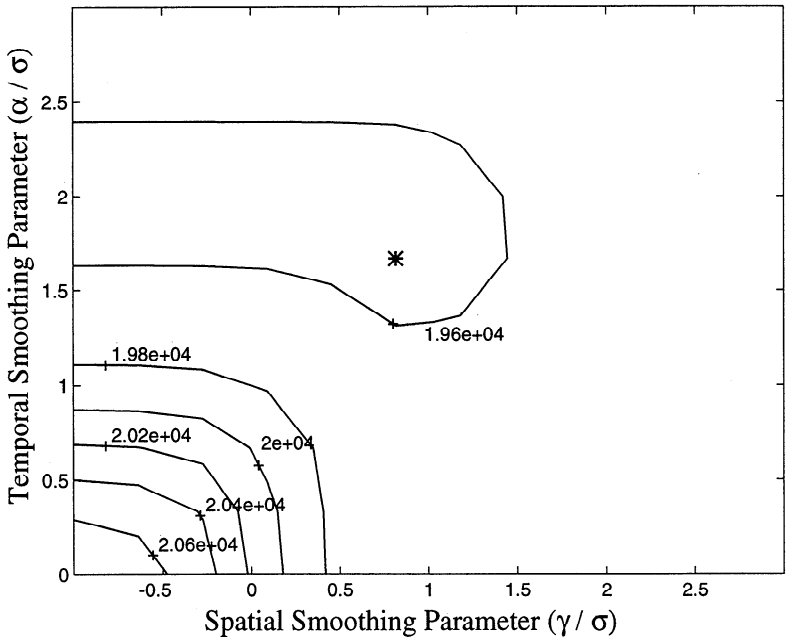

Figure 15. Likelihood surface ($-2\mathcal{L}$) as a function of γ/σ and α/σ. Asterisk marks the minimum, corresponding to the maximum likelihood estimate.

where $\mathbf{0}_N$ is a zero vector of length N. In this way the basis functions with the greatest norm are a priori judged to be zero with small prior variance, whereas basis functions with lesser norm are a priori taken to be zero with much greater prior variance and are thus more loosely constrained. Note that in practice we truncate the spectrum of eigenvalues, reducing the number of independent basis functions, in order to ensure that numerically unstable components are not considered in the solution.

The proportionality constant γ^2 scales the overall size of $\Sigma_{1\,|\,0}$ and thus controls the weight put on fitting the data versus minimizing the spatial norm of the estimated slip. In the work by *Matthews and Segall* [1993] the corresponding parameter was chosen by cross validation. Here we make use of the overall Bayesian context of the Network Information Filter and estimate γ by maximum likelihood. Thus, for space time inversions it is necessary to estimate three parameters (τ/σ, α/σ, and γ/σ) by maximum likelihood.

5.1 Example 1: Accelerating Slip Patch

Consider a horizontal detachment fault subject to antiplane deformation (Figure 12). As in the earlier examples, slip is only out of plane and there is a single non-zero displacement u_3, which varies only as a function of x_1 and x_2. Displacement at the Earth's surface can be written as

$$u_3(x,t) = -\frac{D}{\pi}\int_0^L \frac{s(\xi,t)d\xi}{(x-\xi)^2+D^2}. \qquad (51)$$

where for notational simplicity we let $x \equiv x_1$. From observations of $u_3(x,t)$ we seek to estimate the fault slip $s(\xi,t)$.

As described above, the inverse problem is regularized by seeking solutions that minimize a spatial norm of the slip. For simplicity, we employ here the $L2$ norm corresponding to the following inner product

$$< f,g >= \int_0^L f(\xi)g(\xi)d\xi. \qquad (52)$$

The representer Φ_i is thus given by

$$\Phi_i = -\frac{1}{\pi}\frac{D}{(x_i-\xi)^2+D^2}. \qquad (53)$$

We generate synthetic data (Figure 13) from a growing slip zone on a horizontal decollement. The true slip and slip rate are shown in Figure 14. Measurement errors and local benchmark motions are added with $\sigma = 3$ mm and $\tau = 1$ mm/yr$^{\frac{1}{2}}$.

In order to accelerate the maximum likelihood optimization we generated preliminary estimates of τ and σ by analyzing each baseline separately assuming steady state deformation (as was done for example by *Langbein and Johnson* [1997]). The median values from the network were $\hat{\tau} = 1.6$ mm/yr$^{\frac{1}{2}}$ and $\hat{\sigma} = 2.9$ mm. As expected, $\hat{\tau}$ overestimates the correct value, as non-steady deformation is included in the benchmark motion in this estimate. The next step was to maximize the likelihood over α/σ, and γ/σ. This yielded estimates of $\hat{\alpha} = 294$, and $\hat{\gamma} = 0.029$ (the latter being the minimum value allowed). Given these estimates, a full network analysis of the likelihood yielded an improved estimate of the random walk variance $\hat{\tau} = 0.63$, which is within 40% of the correct value. Finally, α/σ, and γ/σ are recomputed with the updated value of $\hat{\tau}$. The loglikelihood surface as a function of α/σ, and γ/σ is shown in Fig-

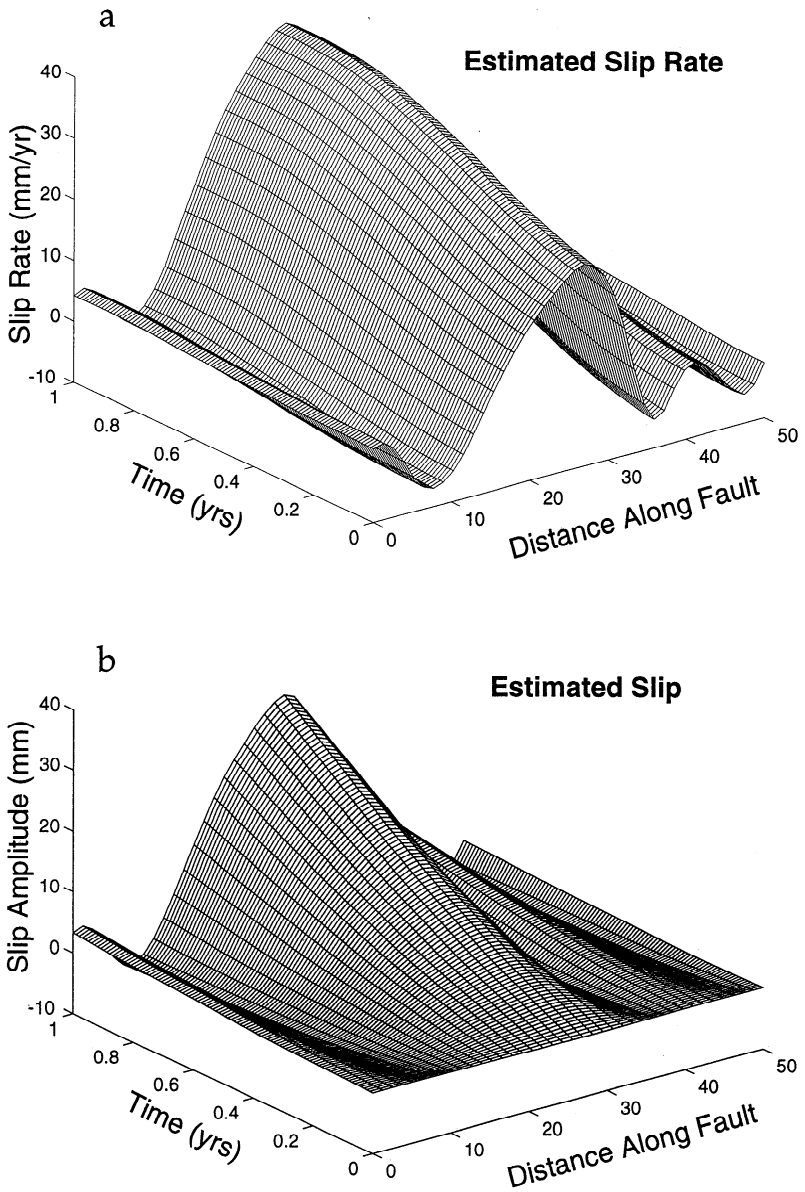

Figure 16. Estimated (a) slip rate and (b) slip, for propagating slip event corresponding to the data shown in Figure 13. Hyperparameters estimated by maximum likelihood correspond to $\hat{\tau} = 0.63, \hat{\sigma} = 2.94, \hat{\alpha} = 136.5$, and $\hat{\gamma} = 19.35$. Compare to true slip and slip velocity shown in Figure 14.

ure 15. Maximum likelihood estimates are $\hat{\alpha} = 136.5$ and $\hat{\gamma} = 19.35$.

The slip and slip rate estimated by the Network Inversion Filter, using the hyperparameters determined by maximum likelihood, are shown in Figure 16. The filter does a reasonably good job of recovering the true slip event. The maximum slip is essentially correct at 40 mm, and the overall slip distribution is reasonably well approximated. The estimate does contain sidelobes that are not present in the true distribution, and the estimated slip rate does not recover the exponential rate increase very well. We note that the likelihood surface (Figure 15) is relatively flat near the minimum, and in fact a solution with somewhat more spatial smoothing ($\hat{\gamma} = 8.0$) and less temporal smoothing ($\hat{\alpha} = 290.0$) does an even better job of recovering the true slip rate pattern in space and time. This example emphasizes that one must examine a number of solutions corresponding to a range of filter hyperparameters around the maximum likelihood estimates before drawing geophysical interpretations from the inversion results.

5.1 Example 2: Propagating Slip Pulse

We next consider an example with a slipping zone that propagates from left to right across the horizontal decollement (Figure 17). Data are generated with errors of $\sigma = 3$ mm and $\tau = 1$ mm/yr$^{\frac{1}{2}}$, as before (Figure 18). The maximum likelihood calculation proceeds as before; however, in this case there are no steady state

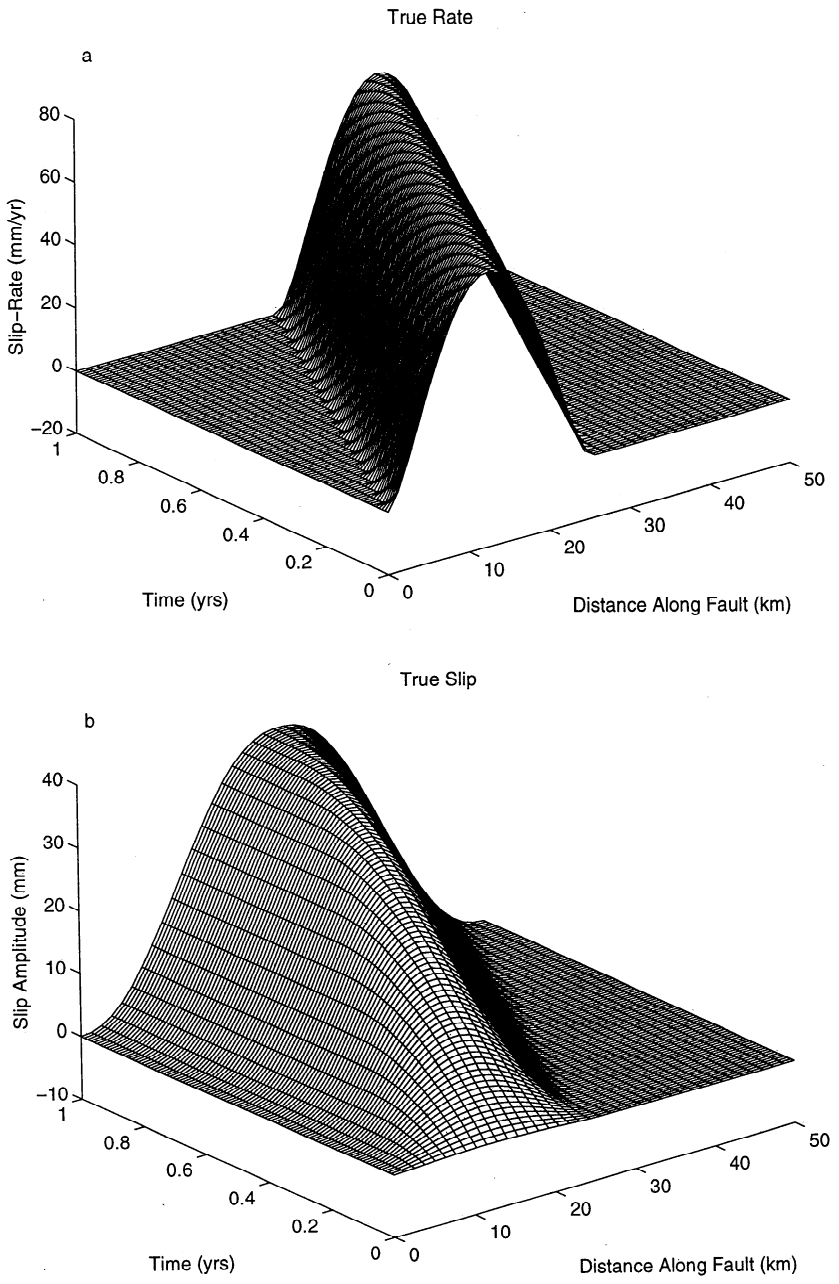

Figure 17. Propagating slip event on a horizontal decollement. (a) True slip rate. (b) True slip.

components to the solution and thus γ is weakly constrained. The likelihood was maximized by the smallest value of γ tested ($\hat{\gamma} = 0.0029$).

The slip and slip velocity estimated by the Network Inversion Filter, shown in Figure 19, do a reasonably good job of recovering the input propagating slip event (Figure 17). The stochastic, non-steady, components of the slip velocity are constrained to be zero at $t = 0$, so that it takes roughly 0.1 years for the estimated slip rate to build up. Following this, the sense of a slip event propagating from left to right across the fault is clearly identifiable in the estimate, and the maximum slip velocity is approximately correct.

As suggested above, the solution is insensitive to γ for sufficiently small values. We find that the estimated slip rate (and slip) is practically indistinguishable for $\hat{\gamma} < 0.003$. For larger values of γ, temporally stationary sidelobes are introduced into the estimated slip rate.

6. Discussion

A number of factors will warrant further analysis. The filtering equations can be simply extended to cover the more realistic case in which each station exhibits random local motions with distinct scale parameters (say τ_j at the jth station). A straightforward attempt at maximum likelihood estimation of the greatly increased set of hyperparameters, however, is not likely to be computationally feasible. One can always estimate approximate values of the τ_j by analyzing each

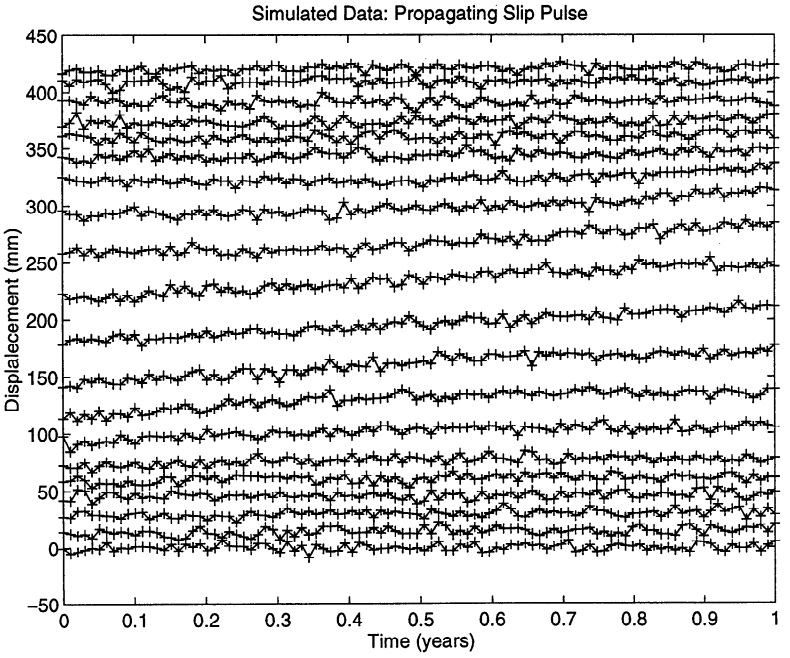

Figure 18. Simulated data over horizontal decollement, with $\sigma = 3$ mm and $\tau = 1$ mm/yr$^{\frac{1}{2}}$. There are 20 baselines total, shown, from west to east, with origins offset vertically for clarity.

baseline separately assuming steady state deformation (as in the work of *Langbein and Johnson* [1997]). It may then be possible to refine these estimates using an extension of the Network Inversion Filter. Seasonal effects are also likely to be present in geodetic measurements. For example, seasonal variations related to rainfall have been observed in the two-color geodimeter data at Parkfield [*Langbein et al.*, 1990]. Such effects introduce local motions that may be random with respect to the direction of the perturbation, but nevertheless temporally correlated. Time domain filtering can be extended to estimate stochastic seasonal variations, although at the expense of added model complexity.

Another issue that must be investigated is the influence of misspecification of the fault geometry on the estimated slip rate pattern. In the work described here we have assumed that the fault geometry is known, and this is never precisely so. Of course, elastic inhomogeneity, anisotropy, and unmodeled inelastic deformation can potentially bias results from the Network In-

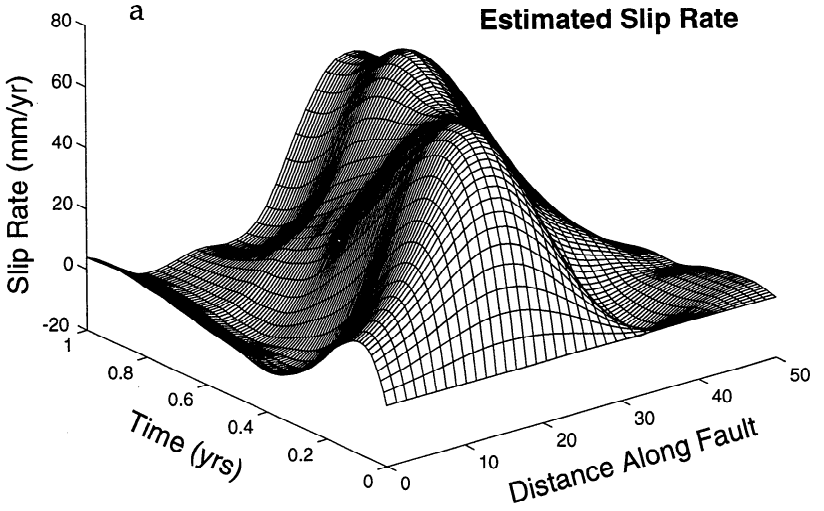

Figure 19. Estimated (a) slip rate, and (b) slip for propagating slip event corresponding to the data shown in Figure 18. Hyperparameters estimated by maximum likelihood correspond to $\hat{\tau} = 0.6, \hat{\sigma} = 2.9, \hat{\alpha} = 1.05 \times 10^3$, and $\hat{\gamma} = 2.9 \times 10^{-3}$. Compare to true slip and slip velocity shown in Figure 17.

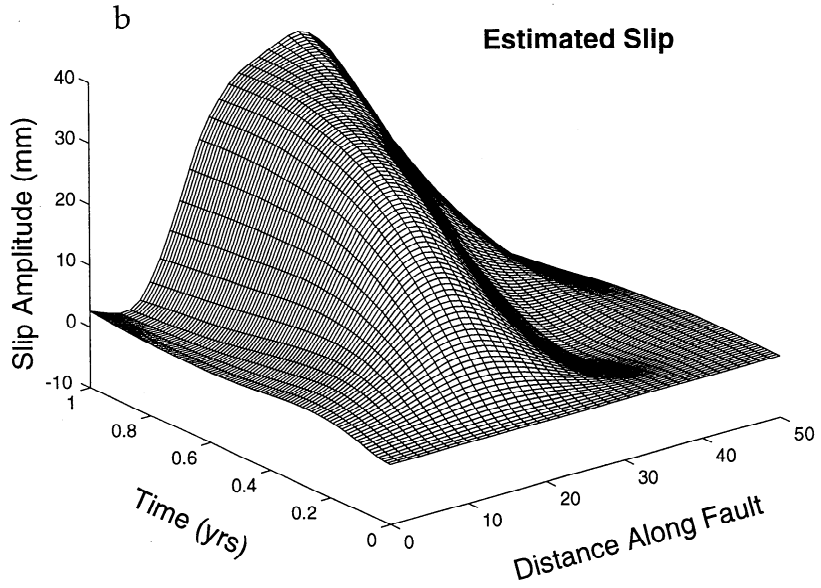

Figure 19. (continued)

version Filter. Ultimately, the power of the technique will be determined by its ability to elucidate processes within the Earth.

7. Conclusion

We have introduced a Network Inversion Filter, which combines elements of linear inverse theory and discrete time Kalman filtering, for estimating the distribution of fault slip in space and time using data from dense, frequently sampled geodetic networks. Although not explicitly considered here, it is possible to include other data types, including data from creep meters and strain meters, so long as the the noise spectra of the data are reasonably well characterized.

The Network Inversion Filter is shown, by simulation, to be capable of recovering nonparametric estimates of fault slip transients in the presence of correlated errors including local benchmark instability. We have also shown that with a sufficient density of stations and signal to noise ratio, it is possible to image fault slip transients, including propagating slip events. While we do not necessarily claim that the transients simulated here all occur in nature, we do suggest that the methods described here provide the appropriate tool for searching for such slip transients. One of the most striking results of this work is the recognition that random benchmark motions can easily obscure significant slip transients (see, for example, Figure 3), suggesting that similar events may have occurred and simply escaped detection. While strain meters have vastly greater sensitivity to deformation than do GPS baseline vector determinations, there are very few places with sufficiently dense strain instrumentation to be able to distinguish between tectonic strain and deformation very local to the instrument.

The Network Inversion Filter leads naturally to automated methods for detecting anomalous departures from steady state deformation. We argue that the Network Inversion Filter provides a rational basis for analyzing data generated by large networks for deformation transients that might precede volcanic eruptions and perhaps earthquakes.

Acknowledgments. We thank the reviewers, J. Savage and C. Goad, and the Associate Editor, R. Bilham, for their thoughtful comments. The bulk of this research was supported directly by the U.S. Geological Survey. We also acknowledge grants from the Southern California Earthquake Center (686889), U.S. Geological Survey NEHRP (1434-95-G-2568) and the National Science Foundation (EAR-95-26910) to Stanford University.

References

Aki, K. and P.G. Richards, *Quantitative Seismology: Theory and Methods*, 932 pp., W. H. Freeman, New York, 1980.

Árnadóttir, T., and P. Segall, The 1989 Loma Prieta earthquake imaged from inversion of geodetic data, *J. Geophys. Res. 99*, 21835-218355, 1994.

Barrientos, S. E., and S. N. Ward, The 1960 Chile earthquake; inversion for slip distribution from surface deformation, *Geophys. J. Int. 103*, 589-598, 1990.

Bennett, R.A., R.E. Reilinger, W. Rodi, Y. Li, M. N. Toksöz, and K. Hudnut, Coseismic fault slip associated with the 1992 M_w 6.1 Joshua Tree, California, earthquake: Implications for the Joshua Tree-Landers earthquake sequence, *J. Geophys. Res. 100*, 6443-6461, 1995.

Blewitt, G., M.B. Heflin, K.J. Hurst, D.C. Jefferson, F.H. Webb, and J.F. Zumberge, Absolute far-field displacements from the 28 June 1992 Landers earthquake sequence, *Nature, 361*, 340-342, 1993.

Bock, Y., et al., Detection of crustal deformation from the Landers earthquake sequence using continuous geodetic measurements, *Nature, 361*, 337-340, 1993.

Bürgmann, R., P. Segall, M. Lisowski, and J.P. Svarc, Postseismic strain following the 1989 Loma Prieta earthquake from repeated GPS and leveling measurements, *J. Geophys. Res., 102*, 4933-4955, 1997.

Dragert, H., and R. D. Hyndman, Continuous GPS monitor-

ing of elastic strain in the northern Cascadia subduction zone, *Geophys. Res. Lett., 22*, 755-758, 1995.

Freymueller, J., N. E. King, and P. Segall, The co-seismic slip distribution of the Landers earthquake, *Bull. Seismol. Soc. Am. 84*, 646-659, 1994.

Fukahata, Y., C. Honsho, and M. Matsu'ura, Crustal movements on Shikoku, southwestern Japan, inferred from inversion analysis of levelling data using ABIC, *Tectonophysics, 257*, 239-252, 1996.

Harris, R. A., and P. Segall, Detection of a locked zone at depth on the Parkfield, California, segment of the San Andreas fault, *J. Geophys. Res., 92*, 7945–7962, 1987.

Harvey, A.C., *Time Series Models*, John Wiley, New York, 1981.

Heflin, M. B., W. I. Bertiger, G. Blewitt, A. P. Freedman, K. J. Hurst, S. M. Lichten, U. J. Lindqwister, Y. Vigue, F. H. Webb, T. P. Yunck, and J. F. Zimberge, Global geodesy using GPS without fiducial sites, *Geophys. Res. Lett., 19*, 131–134, 1992.

Jachens, R.C., W. Thatcher, C. W. Roberts, and R. S. Stein, Correlation of changes in gravity, elevation, and strain in southern California, *Science, 219*, 1215-1217, 1983.

Johnson, H. O., Techniques and Studies in Crustal Deformation, Ph.D. thesis, Univ. of Calif. San Diego, La Jolla, 1993.

Johnson, H. O., and D.C. Agnew, Monument motion and measurements of crustal velocities, *Geophys. Res. Lett., 22*, 2905-2908, 1995.

King, N.E., J.L. Svarc, E.B. Fogelman, W.K. Gross, K.W. Clark, G. D. Hamilton, C. H. Stiffler, and J. M. Sutton, Continuous GPS observations across the Hayward fault, California, 1991-1994, *J. Geophys. Res., 100*, 20,271–20,283, 1995.

Langbein, J., and H. Johnson, Correlated errors in geodetic time series: Implications for time-dependent deformation, *J. Geophys. Res., 102*, 591-603, 1997.

Langbein, J., R. O. Burford, and L. E. Slater, Variations in fault slip and strain accumulation at Parkfield, California; initial results using two-color geodimeter measurements, 1984-1988, *J. Geophys. Res., 95*, 2533-2552, 1990.

Langbein, J., D. Dzurisin, G. Marshall, R. Stein, and J. Rundle, Shallow and peripheral volcanic sources of inflation revealed by modeling two-color geodimeter and leveling data from Long Valley Caldera, California, 1988-1992 *J. Geophys. Res., 100*, 12,487-12,495, 1995.

Linde, A.T., M.T. Gladwin, M.J.S. Johnston, R.L. Gwyther, and R.G. Bilham, A slow earthquake sequence on the San Andreas fault, *Nature, 383*, 65-68, 1996.

Lisowski, M., S. Owen, and P. Segall, The Kilauea volcano, Hawaii, continuous GPS network: Recent results, *Eos, Trans. AGU, 77*, Fall Meeting Suppl., F808, 1996.

Matthews, M. V., On the estimation of fault slip in space and time, Ph.D. thesis, 241 pp., Stanford Univ., Stanford Calif., 1991.

Matthews, M. V., and P. Segall, Detecting transient fault slip with frequently sampled deformation measurements *Eos, Trans. AGU, 69*, 1432, 1988.

Matthews, M. V., and P. Segall, Statistical inversion of crustal deformation data and estimation of the depth distribution of slip in the 1906 earthquake, *J. Geophys. Res., 98*, 12,153–12,163, 1993.

Miyazaki, S., H. Tsuji, Y. Hatanaka, Y. Abe, A. Yoshimura, K. Kamada, K. Kobayashi, H. Morishita, and Y. Iimura, Establishment of the nationwide GPS array (GRAPES) and its inital results on the crustal deformation of Japan, *Bull. Geog. Surv. Inst. Jpn., 42*, 27-41, March 1996.

Parker, R. L, *Geophysical Inverse Theory*, 386 pp., Princeton Univ. Press, Princeton, N.J., 1994.

Prescott, W. H., N. E. King,and G. Gu, Preseismic, coseismic, and postseismic deformation associated with the 1984 Morgan Hill, California, earthquake, in *The 1984 Morgan Hill, California Earthquake*, edited by J. H. Bennett and R. W. Sherburne, *Spec. Pub. Calif. Div. Mines and Geol 68*, 137-148, 1984.

Rauch, H.E., F. Tung, and C. T. Striebel, Maximum likelihood estimates of linear dynamic systems, *AIAA J., 3*, 1445-1450, 1965.

Savage, J. C. and M. Lisowski, Interseismic deformation along the San Andreas Fault in Southern California, *J. Geophys. Res., 100*, 12,703-12,717, 1995.

Savage, J.C., M. Lisowski, and J.L. Svarc, Postseismic deformation following the 1989 (M= 7.1) Loma Prieta, California, earthquake, *J. Geophys. Res. 99*, 13757-13765, 1994.

Segall, P. and R. Harris, Slip deficit on the San Andreas fault at Parkfield, California, as revealed by inversion of geodetic data, *Science, 233*, 1409–1413, 1986.

Shen, Z.K., D.D. Jackson, Y. Feng, M. Cline, M. Kim, P. Fang, and Y. Bock, Postseismic deformation following the Landers earthquake, California, 28 June 1992, *Bull. Seismol. Soc. Am., 84*, 780-791, 1994.

Shimada, S., and Y. Bock, Crustal deformation measurements in central Japan determined by a Global Positioning System fixed point network, *J. Geophys. Res. 97*, 12437-12455, 1992.

Shimada, S., Y. Fujinawa, S. Sekiguchi, S. Ohmi, T. Eguchi, and Y. Okada, Detection of a volcanic fracture in Japan using Global Positioning System measurements, *Nature, 343*, 631-633, 1990.

Tsuji, H., Y. Hatanaka, T. Sagiya, and M. Hashimoto, Coseismic crustal deformation from the 1994 Hakkaido-Toho-Oki earthquake monitored by a nationwide continuous GPS array in Japan, *Geophys. Res. Lett., 22*, 1669-1672, 1995.

Wald, D.J., and T.H. Heaton, Spatial and temporal distribution of slip for the 1992 Landers, California, earthquake, *Bull. Seismol. Soc. Am., 84*, 668-691, 1994.

Wyatt, F. K., Displacement of surface monuments: Horizontal motion, *J. Geophys. Res., 87*, 979-989, 1982.

Wyatt, F. K., Displacement of surface monuments: Vertical motion, *J. Geophys. Res., 94*, 1655-1664, 1989.

Mark Matthews, Department of Mathematics, Massachusetts Institute of Technology, Cambridge MA, 02139. (e-mail: mmatthews@worldstreet.com)

P. Segall, Department of Geophysics, Stanford University, Stanford, CA 94305. (e-mail: segall@geo.stanford.edu)

(Received February 25, 1997; revised June 6, 1997; accepted June 17, 1997.)